

Journal of Biomedical Optics

BiomedicalOptics.SPIEDigitalLibrary.org

***In situ* visualization of intracellular morphology of epidermal cells using stimulated Raman scattering microscopy**

Mariko Egawa
Kyoya Tokunaga
Junichi Hosoi
Shinya Iwanaga
Yasuyuki Ozeki

Mariko Egawa, Kyoya Tokunaga, Junichi Hosoi, Shinya Iwanaga, Yasuyuki Ozeki, “*In situ* visualization of intracellular morphology of epidermal cells using stimulated Raman scattering microscopy,” *J. Biomed. Opt.* **21**(8), 086017 (2016), doi: 10.1117/1.JBO.21.8.086017.

SPIE.

In situ visualization of intracellular morphology of epidermal cells using stimulated Raman scattering microscopy

Mariko Egawa,^{a,*} Kyoya Tokunaga,^b Junichi Hosoi,^a Shinya Iwanaga,^a and Yasuyuki Ozeki^{b,*}

^aShiseido Global Innovation Center, 2-2-1 Hayabuchi, Tsuzuki-ku, Yokohama, Kanagawa 224-0025, Japan

^bThe University of Tokyo, Department of Electrical Engineering and Information Systems, 7-3-1 Hongo, Bunkyo-ku, Tokyo 113-8656, Japan

Abstract. Visualization of epidermal cells is important because the differentiation patterns of keratinocytes (KCs) are considered to be related to the functions and condition of skin. Optical microscopy has been widely used to investigate epidermal cells, but its applicability is still limited because of the need for sample fixation and staining. Here, we report our staining-free observation of epidermal cells in both tissue and culture by stimulated Raman scattering (SRS) microscopy that provides molecular vibrational contrast. SRS allowed us to observe a variety of cellular morphologies in skin tissue, including ladder-like structures in the spinous layer, enucleation of KCs in the granular layer, and three-dimensional cell column structures in the stratum corneum. We noticed that some cells in the spinous layer had a brighter signal in the cytoplasm than KCs. To examine the relevance of the observation of epidermal layers, we also observed cultured epidermal cells, including KCs at various differentiation stages, melanocytes, and Langerhans cell-like cells. Their SRS images also demonstrated various morphologies, suggesting that the morphological differences observed in tissue corresponded to the cell lineage. These results indicate the possible application of SRS microscopy to dermatological investigation of cell lineages and types in the epidermis by cellular-level analysis. © 2016 Society of Photo-Optical Instrumentation Engineers (SPIE) [DOI: 10.1117/1.JBO.21.8.086017]

Keywords: imaging; keratinocyte differentiation; Langerhans cells; stimulated Raman scattering.

Paper 160233R received Apr. 12, 2016; accepted for publication Aug. 10, 2016; published online Aug. 31, 2016.

1 Introduction

Skin is the largest organ in the body and generally classified into three layers: the epidermis at the outermost, dermis, and subcutaneous tissue on the inner side. Among these layers, epidermis is important because it acts as a barrier against the dry environment by prevention of water evaporation, and against harmful external substances. Epidermis consists of four distinct sublayers: the stratum corneum (SC), granular layer, spinous layer, and basal layer from outer to inner sublayers. Cell types, morphology, components, and functions vary among these skin layers. For example, SC is responsible for the barrier function. The basal layer is the only active layer in the epidermis, which has proliferating cells. Epidermis consists mainly of keratinocytes (KCs) and less abundant melanocytes (MCs), Langerhans cells (LCs), and α -dendritic cells.¹ KCs in the basal layer are in the growth phase. The KCs then undergo morphological changes during differentiation as they transit through the epidermis from the spinous layer to SC. The differentiation patterns of KCs are considered to be related to skin conditions.² The enucleated phase of the granular layer is particularly important,^{3,4} because the degree of nuclear digestion in KCs is related to formation of the protective barrier of the skin. Undigested nuclei in KCs of the SC (i.e., parakeratosis) lead to a weak skin barrier function, but the mechanism of DNA degradation during the enucleation process in the final stage of differentiation remains unclear. MCs are pigment cells that produce melanin in the basal layer and protect skin from ultraviolet

radiation. LCs are in the spinous layer, extend long dendritic processes through intercellular spaces between adjacent KCs,⁵ and interact with KCs in a complex manner during cutaneous immune reactions, which defend the body against foreign substances.^{6,7} Thus, the visualization of these epidermal cells is important to better understand skin functions and conditions.

Previous reports on the visualization of these characteristic epidermal cells have used combinations of staining/labeling techniques and optical imaging.^{5,8–11} However, these techniques are limited in their applicability because they rely on the use of fluorescent dyes or proteins. In addition, we should consider the effect of color degradation and cytotoxicity of fluorescent substances on the analysis of biological responses. Recent progress in optical imaging techniques, such as confocal microscopy,¹² multiphoton microscopy,¹³ and optical coherence tomography,¹⁴ has enabled noninvasive visualization and analysis of the structures of skin layers at a particular depth. These noninvasive optical instruments have been partly applied to *in vivo* measurements of human epidermal cells. *In vivo* confocal microscopy, which detects backscattering due to variations in the refractive index at the boundary of cells, has been applied to visualize MCs in the basal layer, because melanin provides a strong contrast due to its large refractive index difference with the surrounding components in KCs.¹² It was also applied to visualization of the morphology of corneal LCs with elongated dendrites.¹⁵ The morphology of KCs has been partly visualized using multiphoton microscopy¹³ and optical coherence tomography.¹⁴

Address all correspondence to: Mariko Egawa, E-mail: mariko.egawa@shiseido.co.jp; Yasuyuki Ozeki, E-mail: ozeki@ee.t.u-tokyo.ac.jp

However, it still appears to be difficult to visualize intracellular morphology and differentiate various epidermal cells using these noninvasive optical methods.

Recently, Raman spectroscopy and microscopy methods have attracted much attention because they provide alternative information based on the molecular vibrational signature. Spontaneous Raman scattering microscopy has been used to analyze epidermal components *in vivo*^{16–18} and to visualize myoblasts during differentiation¹⁹ and nucleic acids and tryptophan in human skin cells.²⁰ A more recent study reported the response of LCs to medical agents.²¹ However, this technique requires a long acquisition time and is rarely applied to skin imaging. In contrast, coherent Raman scattering microscopy techniques,^{22,23} including coherent anti-Stokes Raman scattering microscopy and stimulated Raman scattering (SRS) microscopy,^{24–26} have enabled faster imaging of various functional groups of molecules. In particular, SRS microscopy has led to a variety of applications to biological samples^{27–40} including skin,^{41–44} taking advantage of the capability of SRS microscopy for high-speed image acquisition with vibrational contrast. However, it is still unclear whether SRS can visualize intracellular morphology of various types of epidermal cells and whether SRS can discriminate cell lineages and types in the epidermis.

In this study, we demonstrate SRS imaging of epidermal cells in both skin tissues and culture *in situ* with subcellular spatial distribution. Our detailed investigation of intracellular morphology with vibrational contrast indicates the possibilities of detecting the changes in KC characteristics associated with differentiation and discriminating cell types.

2 Materials and Methods

2.1 Skin tissues

To image the epidermis, we prepared pig and human skin samples as follows.

The left ear of a white pig was purchased from Tokyo Shibaura Zouki Co., Ltd. (Gelding or female; Hybrid of Yorkshire, Large Yorkshire, and Landrace; Tokyo, Japan). The exterior side of the lower part of the ear skin was cut into a rectangular shape (~30 × 100 mm). Hair was removed with scissors, then extra SC was removed with instant adhesive (Aron Alpha®; TOAGOSEI Co. Ltd., Nagoya, Japan) using a glass slide by pressing it to the skin surface for 5 min, then peeling it off. The pig skin tissue was refrigerated until the measurements on sterilized gauze in a 35-mm dish containing a double dilution of antibiotic-antimycotic (15240-062, Gibco®, Life Technologies, Thermo Fisher Scientific K.K., Yokohama, Japan) and 50-fold dilution of gentamycin (G1397010ML, Sigma-Aldrich Co. LLC, St. Louis, Missouri) in PBS (D-PBS (-), Nacalai Tesque Inc., Kyoto, Japan) with the skin surface facing upward.

Human abdominal skin tissues from Caucasian females obtained by reductive abdominal surgery were purchased from Biopredic International (Rennes, France).^{45,46} The human skin tissues were dermatomed with ~400-μm thickness on the production date and transported to Japan. The tissues were refrigerated during transit and until the measurements. Tissues for histology were stored in paraformaldehyde on the production date, then embedded in paraffin maintained between 4°C and 15°C upon arrival in Japan. Deparaffinized 3-μm thick skin tissue sections were used for hematoxylin-eosin (HE) staining.⁴⁷

Paraffin-embedded 4-μm thick human skin tissue sections were used for immunohistochemical staining of LCs and were processed as follows. The sections were rehydrated, incubated in sodium citrate buffer (10 mM, pH 6.0) at 90°C for 5 min for antigen retrieval, then permeabilized with 0.2% Triton X-100 for 45 min. After blocking with 10% normal goat serum, the sections were incubated with a rabbit anti-human CD207 antibody (Sigma-Aldrich Co. LLC), then Alexa Fluor-488 goat anti-rabbit IgG (Life Technologies, Thermo Fisher Scientific K.K.).

2.2 Cell Culture

To image cultured epidermal cells, we prepared KCs, MCs, and LC-like cells (LCLCs). Human epidermal KCs (Kurabo Industries Ltd., Osaka, Japan) were cultured in serum-free CnT-Prime medium (CellnTEC Advanced Cell System AG, Bern, Switzerland) for 2 days at 1 × 10⁵ cells/2 ml in glass-bottom 35-mm dishes. Differentiation was induced by a further 2 days of incubation in Dulbecco's modified Eagle's Essential Medium (Life Technologies, Thermo Fisher Scientific K.K.) supplemented with 10% fetal bovine serum and 2 mM CaCl₂.

Human MCs (Kurabo Industries Ltd.) were cultured in serum-free medium (DermaLife M, Lifeline Cell Technology, Frederick, Maryland) at 5 × 10⁴/2 ml in glass-bottom 35-mm dishes.

LCLCs, whose characteristics are close to those of LCs, were prepared as described previously.⁴⁸ Briefly, cord blood-derived CD34-positive cells (Lonza Group Ltd., Valais, Switzerland) were expanded and seeded at 2 × 10⁴ cells/2 ml in glass-bottom 35-mm dishes. They were cultured for a further 7 days in serum-free CellGroDC medium (CellGenix GmbH, Freiburg, Germany) supplemented with 100 ng/ml granulocyte-macrophage colony-stimulating factor, 20 ng/ml stem cell factor, 50 ng/ml fms-related tyrosine kinase 3 ligand, 2.5 ng/ml tumor necrosis factor-α, and 0.5 ng/ml transforming growth factor-β1. For the last 2 days, 200 ng/ml bone morphogenic protein-7 was added to the medium.

2.3 Stimulated Raman Scattering Microscopy

The details of our SRS microscope have been described previously.^{30,39} Briefly, a Ti:sapphire (Ti:S) laser at 790 nm and a wavelength-tunable Yb fiber (YbF) laser at 1014 to 1046 nm were used as light sources. The power of the Ti:S and YbF lasers at the input of the laser scanners was 120 mW each. SRS images (80 × 80 μm; 500 × 500 pixels; transmission mode; horizontal spatial resolution of ~1 μm) were acquired in the wavenumber range of 2800 to 3100 cm⁻¹ that corresponds to the C-H stretching region. The frame rate of the microscope was 30 frames/s. Images were accumulated to improve the signal-to-noise ratio. Specifically, the numbers of accumulation were 10 to 20 in the continuous wavenumber scanning mode and 300 in the discrete scanning mode. The resultant acquisition time was 30 to 60 s and 30 s, respectively. The wavelength dependence of the intensity of the YbF laser was measured on each measurement day and used for calibration.

2.4 Stimulated Raman Scattering Imaging of Skin Tissues and Cultured Cells

Skin tissue sections of <300-μm thickness were immersed in PBS, mounted onto a cover slip, and sandwiched with another coverslip. The sections imaged in the cross-section had a

Table 1 Measurement profiles.

No.	Material origin	Anatomical site	Age	Surgery date	Production date	Measurement date	Storage condition
M1	White pig	Left ear	6 months	—	August 5, 2014 AM (JST)	August 6, 2014 (JST)	Refrigerated at 4°C
M2	Caucasian female	Abdomen	33 years	October 23, 2014 at 15:00 (GMT +2)	October 24, 2014 at 10:45 (GMT +2)	October 29, 2014 (JST)	Refrigerated at 4°C
M3	Cultured cells	—	—	—	November 26, 2014 (JST)	November 26, 2014 (JST)	—
M4	Caucasian female	Abdomen	52 years	February 19, 2015 at 9:45 (GMT +2)	February 19, 2015 at 14:35 (GMT +2)	February 24, 2015 (JST)	Refrigerated at 4°C
M5	Cultured cells	—	—	—	June 24, 2015 (JST)	June 24, 2015 (JST)	—

depth-step size of 1 μm for the SC and 2 μm for other parts of the epidermis. The samples were placed on the microscope stage so the laser beam entered from the surface of the SC. KCs in the growth phase, differentiated KCs, MCs, and LCLCs cultured in glass-bottom 35-mm dishes were imaged in the cross-section. Measurement profiles are shown in Table 1.

The Raman shift was scanned either continuously or discretely. In continuous scanning, the Raman shift was changed in the 2800 to 3100 cm^{-1} range with a step of 3.3 cm^{-1} to acquire 91 SRS spectral images. In discrete scanning, we acquired SRS images at 2850 cm^{-1} (CH_2 symmetric stretching), 2930 cm^{-1} (CH_3 symmetric stretching), and 3010 cm^{-1} (=C—H stretching). Note that the SRS spectra of biological molecules significantly overlap in the C—H stretching region. For example, the SRS signal of lipids appears at both 2850 and 2930 cm^{-1} to almost an equal degree, and that of proteins has a peak at 2930 cm^{-1} . Nevertheless, we used the above three wavenumber images as attributable mainly to lipids, primarily proteins, and unsaturated lipids, respectively, as reported by previous studies.^{23,36,40,43,44} Normalization of SRS spectra for each measurement day (M) was performed using the wavelength dependence of the intensity of the YbF pulses shown in Fig. 1. As the reference spectrum of the YbF pulses, we used that of the last measurement day (M5). SRS images were processed with

ImageJ software (ImageJ 1.48v; National Institutes of Health, Bethesda, Maryland) and IMARIS software (Imaris 8.1.2; Bitplane AG, Zurich, Switzerland).

3 Results and Discussion

3.1 Intracellular Morphologies of Skin Tissue

We first acquired a *z*-stack of horizontal SRS images of skin tissues *in situ* in the discrete scanning mode. Figure 2 shows horizontal plane SRS images of the epidermis in the normal area of pig tissue. We can see lipid-rich granules in the cytoplasm [Fig. 2(a1)] in the lipid (2850 cm^{-1}) image of the granular layer and the accumulation of lipids and proteins imaged at 2850 and 2930 cm^{-1} , respectively, in the nucleus [Fig. 2(a2)]. Protein (2930 cm^{-1}) and strong lipid (2850 cm^{-1}) signals surrounding the nucleus could also be visualized in the upper part of the spinous layer [Figs. 2(b1) and 2(c1)]. Ladder-like structures between cells [Figs. 2(c2) and 2(c3)] were observed as bright protein signals in the spinous layer. In Fig. 3, Video 1 shows the whole *z*-stack of merged (2850 cm^{-1} , red; 2930 cm^{-1} , blue) images of a normal area, and Video 2 shows it in a reddened area of pig tissue. The accumulation of lipids and proteins in the nucleus in the upper part of the spinous and granular layers was not observed in the reddened area, suggesting disorganization of the KC differentiation process. A difference in epidermal thickness was also observed between the normal area (Video 1) and reddened area (Video 2). Thus, the characteristics of intracellular morphology during KC differentiation were visualized in pig tissue *in situ*.

We next visualized the KC differentiation process in human skin tissues. Figure 4 shows SRS images of human epidermis at the abdominal site of a 52-year-old Caucasian female on M4. Merged color images were produced with 2850 cm^{-1} , red; 2930 cm^{-1} , blue; 3010 cm^{-1} , yellow. Similar to pig tissues, we observed intracellular morphologies such as lipid-rich granules in the granular layer [Fig. 4(b1)], accumulation of lipids and proteins in the nucleus [Fig. 4(c1)], a strong lipid signal surrounding the nucleus [Fig. 4(d1)], and the existence of structures within nuclei [Fig. 4(d2)]. In addition, a relatively high intensity was observed in the SC [Fig. 4(a1)] of the lipid image. These intracellular morphologies were also observed in another sample of human skin tissue aged 33 years on M2 as well as five additional human tissues in several fields of view (data not shown).

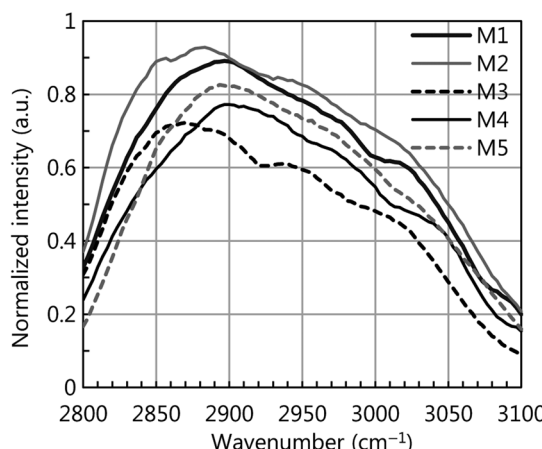


Fig. 1 Wavenumber dependence of the intensity of Stokes pulses. The wavenumber dependence at each measurement day (M1 to M5 in Table 1).

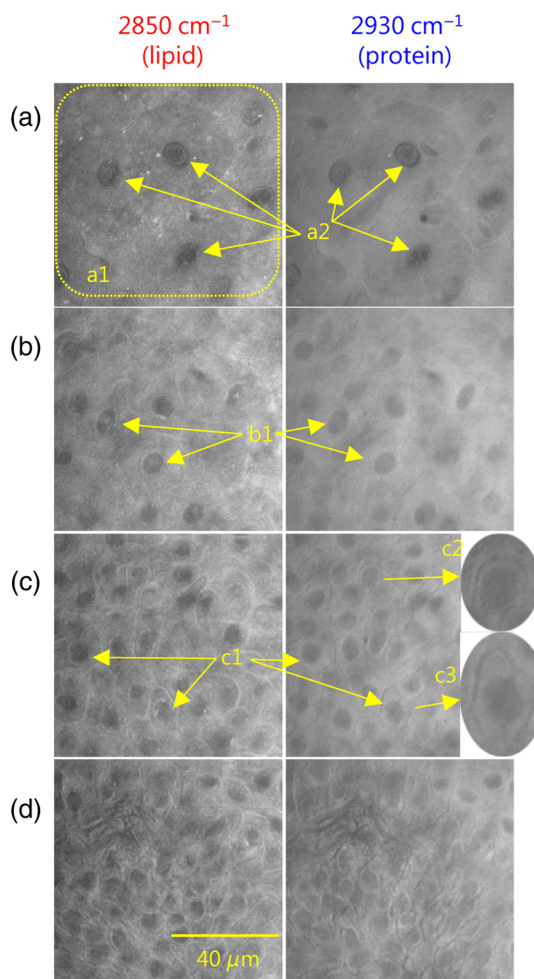


Fig. 2 SRS images of pig epidermis at various depths. (a) Approximately 4 μm under the bottom of the SC. This layer is assumed to be the granular layer. (b) Ten micrometers under the bottom of the SC. This layer is assumed to be the upper part of the spinous layer. (c) Sixteen micrometers under the bottom of the SC. This layer is assumed to be the middle part of the spinous layer. (d) Twenty-two micrometers under the bottom of the SC. This layer is assumed to be the basal layer of a normal area in pig skin.

Thus, intracellular morphological changes during KC differentiation were also observed in human tissues.

By comparing them with skin morphology,¹ ladder-like structures between cells [Figs. 2(c2) and 2(c3)] in the spinous

layer can be attributed to adhesion structures such as desmosomes. Protein and strong lipid SRS signals surrounding the nucleus in the upper part of the spinous layer [Fig. 2(b1) and 2(c1), Fig. 4(d1)] reflected the endoplasmic reticulum (ER), which synthesizes membrane proteins, and lipid-rich granules in the granular layer [Figs. 2(a1) and 4(b1)] reflected lamellar granules in which lipids accumulate. In addition, a relatively high intensity in the lipid image of the SC [Fig. 4(a1)] can be attributed to intercellular lipids, which mainly include ceramides, free fatty acids, and cholesterol.

3.2 Visualization of Morphological Changes in the Final Stage of Keratinocyte Differentiation

Next, we focused on the final stage of KC differentiation, where KCs with digested nuclei form layered structures.¹ Figure 5 shows typical SRS spectra and images of the human SC of a 52-year-old Caucasian female on M4. KCs in the SC had large flattened polygonal features and strong signal intensities of lipids (2850 cm^{-1}) in SRS spectra. Video 3 in Fig. 6 shows the three-dimensional morphology of KCs from the granular layer to the surface of the SC with a depth-step size of 1 μm . The edge of each KC was extracted and applied to rainbow coloring using the find edge tool in ImageJ software after brightness inversion of protein (2930 cm^{-1}) images. Three-dimensional honeycomb structures of KCs at the final stage of the epidermal differentiation process were clearly extracted. The honeycomb structure in the granular layer was not in range with the cell column in the SC in the vertical direction. The three-dimensional morphology of KCs is a biomarker to evaluate skin conditions related to abnormal KC differentiation.¹

3.3 Visualization of the Intracellular Morphology of Cultured Keratinocytes

To reveal the characteristics of KCs in detail, we acquired SRS images of cultured KCs in continuous wavenumber scanning mode. Figure 7(A) shows the obtained SRS spectra and SRS images at 2820 , 2850 , 2930 , and 3010 cm^{-1} of cultured KCs in the growth phase. The SRS image at 2820 cm^{-1} , where no Raman-active vibration is present, is shown, as well as 2850 , 2930 , and 3010 cm^{-1} to confirm that the images were not affected by unwanted artifacts that may originate from two-photon absorption and cross-phase modulation. Merged color images were produced with 2850 cm^{-1} , red; 2930 cm^{-1} , blue; 3010 cm^{-1} , yellow. Signals associated with nuclear structures [Fig. 7(A-b)], such as the nucleolus, heterochromatin, and

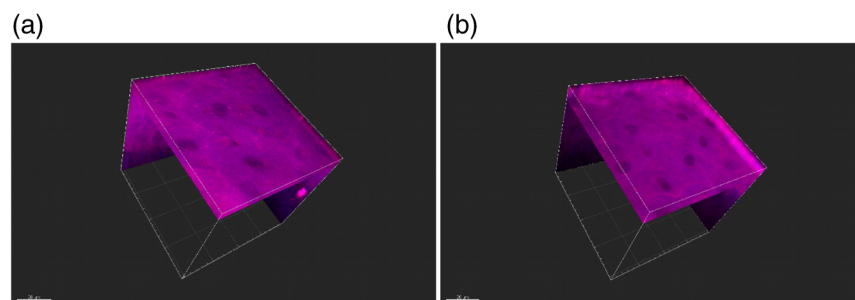


Fig. 3 Z-stack merged (2850 cm^{-1} , red; 2930 cm^{-1} , blue) images of pig skin tissues. (a) Normal area of pig skin (Video 1) and (b) reddened area of pig skin (Video 2) (Video 1, MPEG, 6.39 MB [URL: <http://dx.doi.org/10.1117/1.JBO.21.8.086017.1>]; Video 2, MPEG, 6.54 MB [URL: <http://dx.doi.org/10.1117/1.JBO.21.8.086017.2>]).

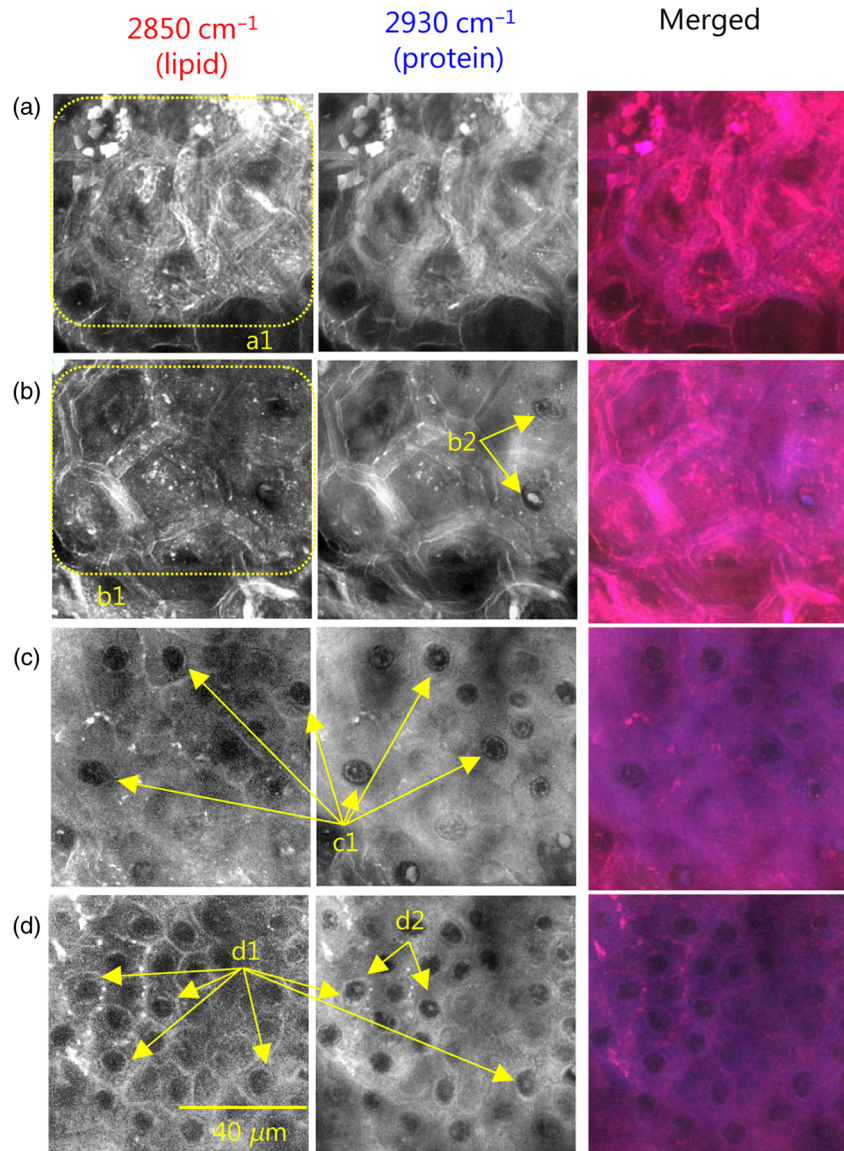


Fig. 4 SRS images of human epidermis of the abdominal site of a 52-year-old Caucasian female at various depths. (a) The SC. (b) Sixteen micrometers under the top of the SC. This layer is assumed to be the granular layer. (c) Twenty-six micrometers under the top of the SC. This layer is assumed to be the upper part of the spinous layer. (d) Thirty-four micrometers under the top of the SC. This layer is assumed to be the middle part of the spinous layer. Merged color images were produced with 2850 cm^{-1} , red; 2930 cm^{-1} , blue; 3010 cm^{-1} , yellow.

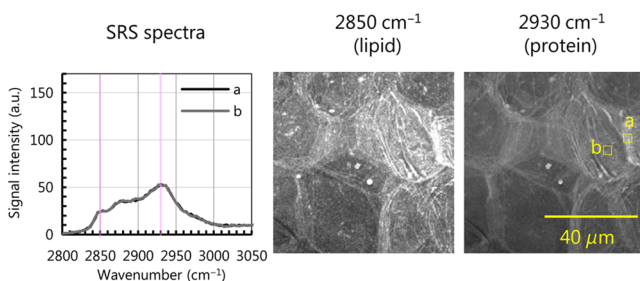


Fig. 5 Typical SRS spectra and images of human SC at the abdominal site of a 52-year-old Caucasian female.

euchromatin, were clearly detected in protein images at 2930 cm^{-1} . These signals can partly include histones and DNA in chromatin⁴⁴ because of the spectral shift to high wavenumbers for nuclear structures such as the nucleolus [Fig. 7(A-b)] compared with the cytoplasm [Fig. 7(A-c)]. The SRS spectra of nuclei in KCs [Fig. 7(A-a)] were identifiable as dark areas in 2850 , 2930 , and 3010 cm^{-1} images, and had a lower brightness level across the whole spectral range, indicating lower protein or DNA content. A bright signal corresponding to the region surrounding the nucleus [Fig. 7(A-d)] was observed in the 2850 cm^{-1} image. This region also had a peak in the spectrum at 2877 cm^{-1} because the Raman spectrum of lipids typically ranges from $2850 - 2920\text{ cm}^{-1}$. We can see that the cell in the nondividing phase [Fig. 7(A-e)] exhibited a much stronger

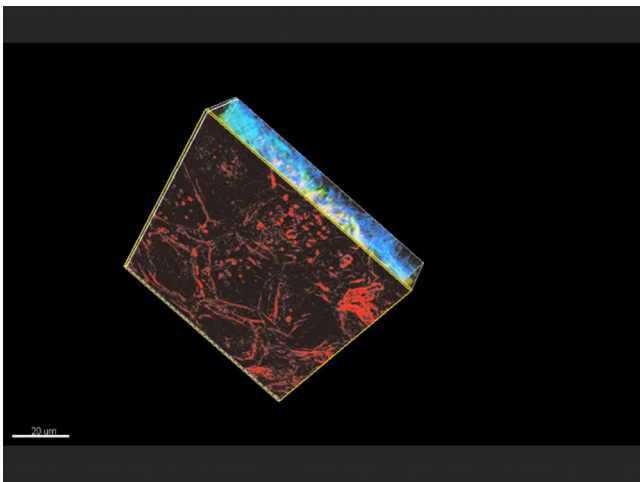


Fig. 6 Three-dimensional morphology of keratinocytes (KCs) from the granular layer to the surface of the SC at the abdominal site of a 52-year-old Caucasian female, which is similar to Fig. 5. (Video 3, MPEG, 5.75 MB [URL: <http://dx.doi.org/10.1111/1.JBO.21.8.086017.3>]).

signal than that in the division phase [Fig. 7(A-f)]. Presumably, this lipid-rich region may reflect the remnants of focal adhesions.

We next obtained SRS images associated with the differentiation of KCs. Figures 7(B) and 7(C) show differentiated KCs at different locations of a culture dish. Presumably, differentiation was further progressed at Figure 7C than 7B, considering the cell size. We can see a lipid-rich, flat-layered structure surrounding the nuclei in Figs. 7(B-d) and 7(C-d). Bright regions observed around nuclei in 2850, 2930, 3010 cm⁻¹ images

were larger in differentiated KCs [Figs. 7(B-d) and 7(C-d)] than in growing cells [Fig. 7(A-d)]. Their morphology and spectra were different from the lipid-rich granular structure shown in Fig. 7(A). They [Figs. 7(B-d) and 7(C-d)] were assumed to reflect the ER. In addition, a bright mottled pattern was observed throughout the cytoplasm of differentiated KCs only [Fig. 7(C)] in both lipid and protein (2850, 2930 cm⁻¹) images. Possibly, these lipid-rich structures were lamellar granules. The differentiated KCs shown in Figs. 7(B) and 7(C) may correspond to cells in the granular layer of skin tissue,¹ which actively synthesizes intercellular lipids and contains them within lamellar granules. The z-stacks of merged images of KCs are shown in Videos 4–6 of Fig. 8. In KCs at the growth phase (Video 4), we can clearly see the typical cylindrical structures that are thought to be the remnant of focal adhesions in the regions surrounding the nucleus. However, in the three-dimensional images of differentiated KCs (Videos 5 and 6), the vertical profiles were different and we cannot see the lipid-rich structures. These intracellular structures were also observed in the other 10 dishes of KCs at the growth phase and eight dishes of differentiating KCs in several fields of view (data not shown). The results indicate that the morphological differences associated with KC differentiation were clearly observed in cultured cells and skin tissues by SRS microscopy.

3.4 Possible Discrimination of Epidermal Cell Types

In the spinous layer of skin tissues, we observed the characteristic cells indicated by the arrows in Fig. 9, which have different intracellular morphologies from those of KCs. This subset of cells exhibited a brighter cytoplasmic signal than the surrounding KCs in lipid and protein (2850, 2930 cm⁻¹) images, and a more pronounced nuclear signal in the protein (2930 cm⁻¹) image than KCs. We speculated that these cells were possibly

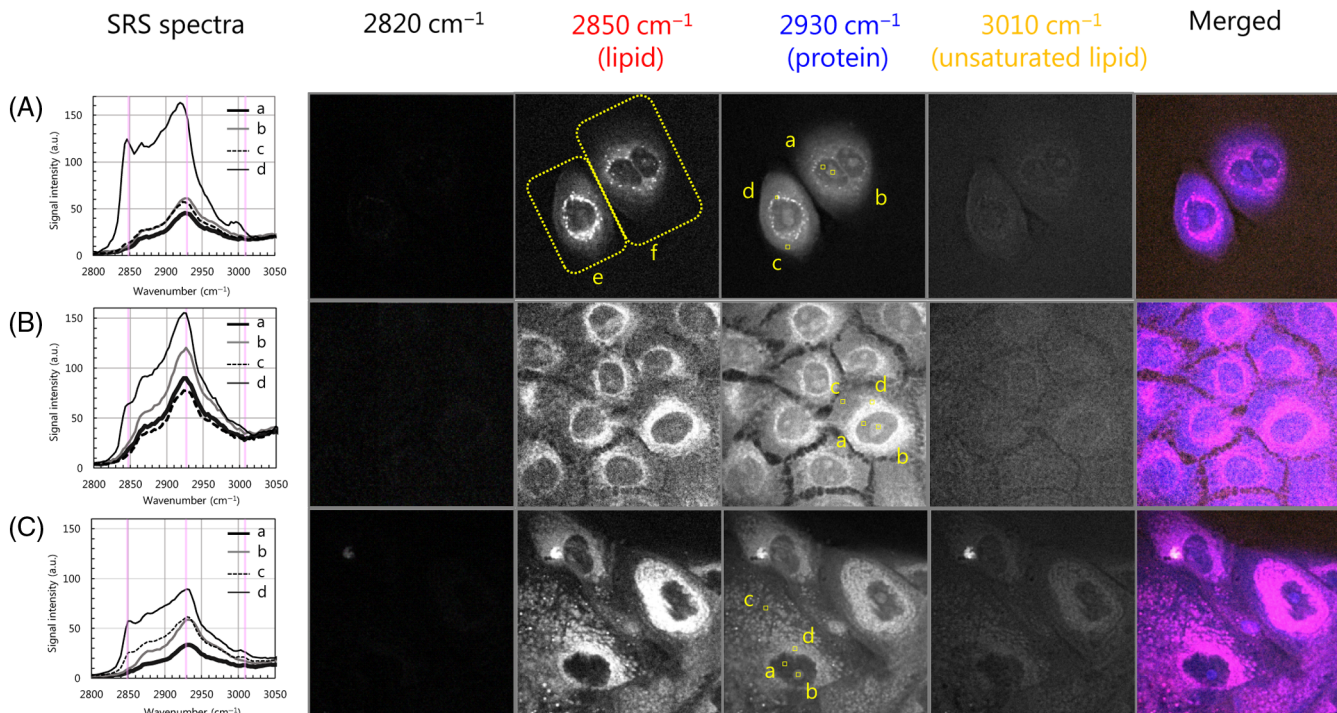


Fig. 7 SRS spectra and images of cultured KCs. (A) KCs in the growth phase and (B, C) differentiated KCs obtained on measurement day (M) 5. Merged color images were produced with 2850 cm⁻¹, red; 2930 cm⁻¹, blue; 3010 cm⁻¹, yellow.



Fig. 8 Z-stack merged images of cultured KCs. (a) KCs in the growth phase (Video 4) and (b, c) differentiated KCs (Video 5, 6) (Video 4, MPEG, 2.04 MB [URL: <http://dx.doi.org/10.1117/1.JBO.21.8.086017.4>]; Video 5, MPEG, 2.24 MB [URL: <http://dx.doi.org/10.1117/1.JBO.21.8.086017.5>]; Video 6, MPEG, 2.10 MB [URL: <http://dx.doi.org/10.1117/1.JBO.21.8.086017.6>]).

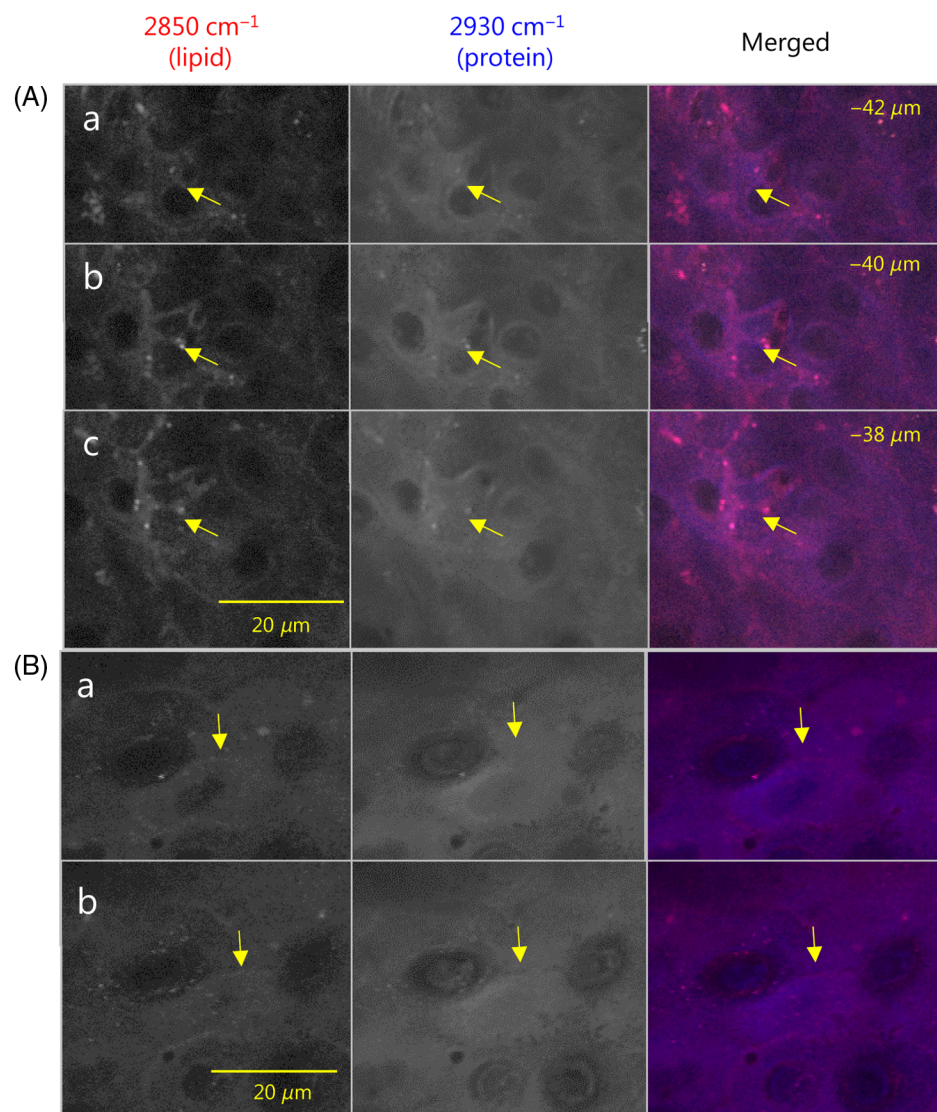


Fig. 9 Characteristic epidermal cells in human tissues. Merged color images were produced with 2850 cm^{-1} , red; 2930 cm^{-1} , blue; 3010 cm^{-1} , yellow. (A) The depth was 38 to 42 μm under the top of the SC. This layer was assumed to be a spinous layer at an abdominal site of a 52-year-old Caucasian female. (B) The upper part of spinous layers at an abdominal site of a 33-year-old Caucasian female. A subset of cells (arrows) assumed to be LCs exhibited a brighter cytoplasmic signal than that of surrounding KCs in lipid and protein ($2850, 2930\text{ cm}^{-1}$) images and a more pronounced nuclear signal in the protein (2930 cm^{-1}) image.

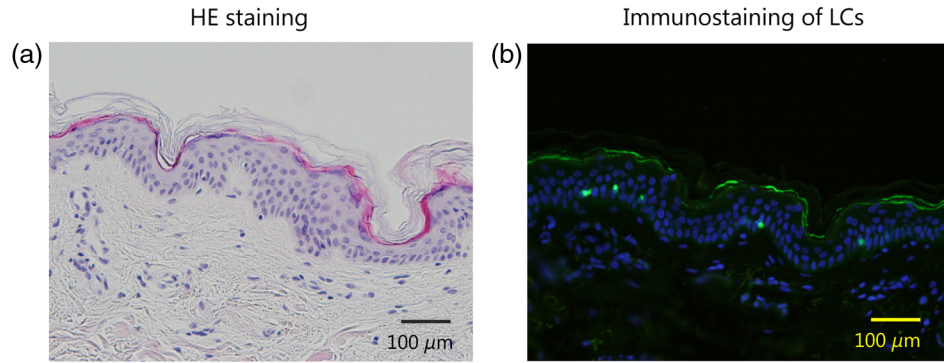


Fig. 10 HE staining and immunostaining of LCs of skin tissues from the abdominal site of a Caucasian female aged 52 years. Images corresponding to HE staining (a), immunostaining of LCs in green together with nuclear staining in blue (b). Immunostaining of LCs showed that the number of LCs in a $80 \times 80 \mu\text{m}$ horizontal plane of human epidermis ranged from 0 to 2.

LCs. The location of these cells was consistent with immunostaining shown in Fig. 10, in which LCs were found within the middle-to-lower part of the spinous layer. These cells were also observed in SRS images of an additional five human skin tissues in several fields of view (data not shown).

For comparison with *in situ* SRS images, we investigated the intracellular morphologies of cultured LCLCs. Figure 11(A) shows LCLCs with a stretched shape, and Fig. 11(B) shows those with a circular shape. Merged color images were produced with 2850 cm^{-1} , red; 2930 cm^{-1} , blue; 3010 cm^{-1} , yellow. The 2930 cm^{-1} images of LCLCs revealed uniformly bright areas in the cytoplasm [Figs. 11(A-b) and 11(B-b)], which could be attributed to the presence of proteins. Interestingly, nuclear

components were rarely observed in LCLCs, which were different from KCs (Fig. 7). LCLCs of both morphologies exhibited these similar intracellular structures. This property also supports our above-mentioned hypothesis that the subset of cells observed in skin tissues may be LCs. Furthermore, we observed clear granular particles in the cytoplasm of LCLCs [Figs. 11(A-b) and 11(B-b)] in both 2850 and 2930 cm^{-1} images. Because LCs have specific cellular compartments related to their antigen presenting function, these lipid-rich granules might possibly represent such compartments, although the origin of the granular particles is still not completely clear at present.

In addition, MCs showed highly characteristic intracellular morphologies. The cytoplasm of MCs showed bright mottled

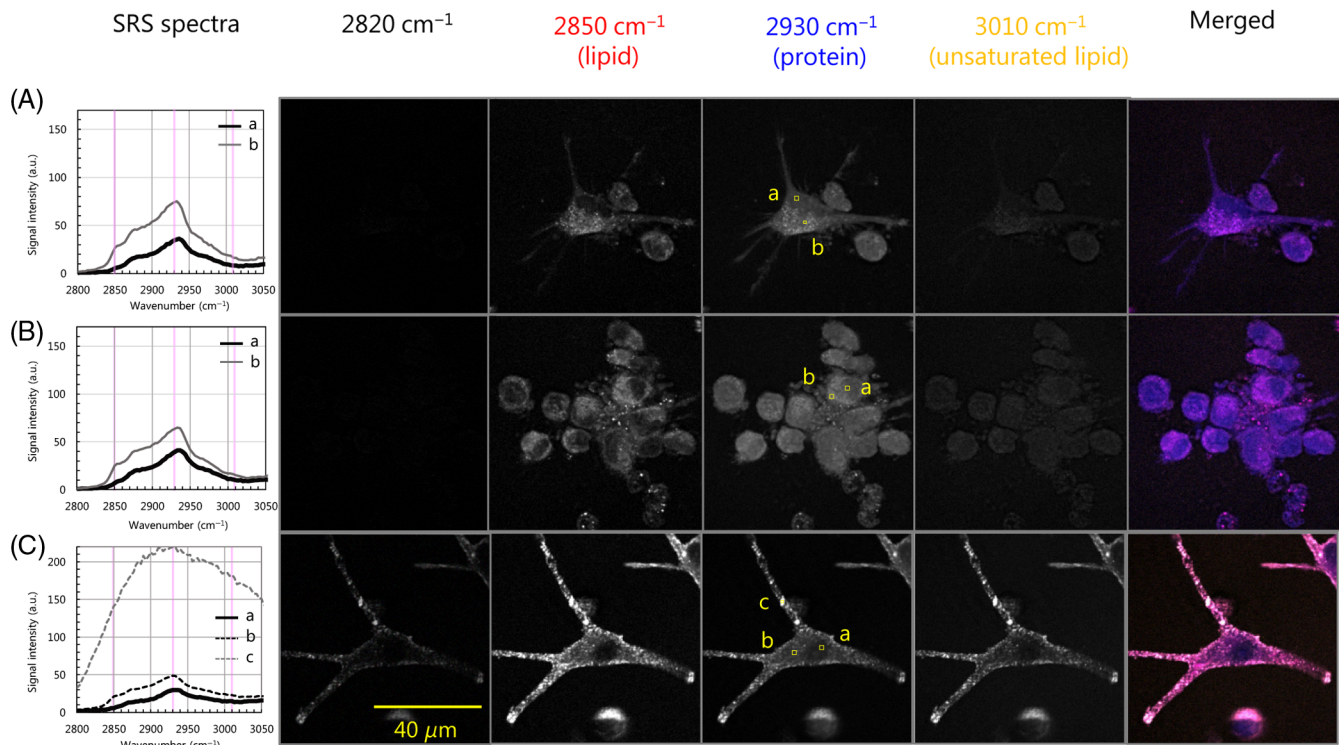


Fig. 11 SRS spectra and images of LCLCs and MCs on M3. (A) LCLCs exhibiting a stretched shape, (B) LCLCs exhibiting a circular shape, and (C) MCs. The Raman shift was set to 2820 cm^{-1} , 2850 cm^{-1} (CH_2), 2930 cm^{-1} (CH_3), and 3010 cm^{-1} ($=\text{CH}$). Merged color images were produced with 2850 cm^{-1} , red; 2930 cm^{-1} , blue; 3010 cm^{-1} , yellow.

spots [Fig. 11(C-c)] compared with the base area of the cytoplasm [Fig. 11(C-b)] in all wavenumber images. The bright spots [Fig. 11(C-c)] indicated a typical spectral pattern of two-photon absorption, showing high brightness levels over the whole wavenumber range, which could be attributed to the presence of chromospheres such as melanin or melanosomes. Therefore, we could distinguish MCs from KCs and LCLCs using these two-photon absorption images.

Here, we showed that KCs, LCLCs, and MCs have different SRS spectra and morphologies. These characteristics were also observed in the other eight dishes of LCLCs and 12 dishes of MCs in several fields of view (data not shown). Results from both skin tissues and cultured epidermal cells indicated that we could discriminate cell types using intracellular morphologies.

4 Conclusions

In this study, we have shown that SRS microscopy reveals the various morphological features of intracellular structures with vibrational contrast, including differentiation and proliferation of KCs in both skin tissues and cultured cells, and differences in epidermal cell types. These results indicate the possibility of cellular-level analysis without labeling using SRS microscopy, which will be useful in dermatological research to elucidate the mechanisms of skin disorders and cutaneous immune reactions. Although our SRS microscope operated in transmission mode in this study, we may be able to discriminate cell lineages and types *in vivo* by incorporating epidetection mode,^{41,43} which will be of great importance in skin diagnosis applications.

Acknowledgments

We thank Ms. Yuki Ogura for her kind support with handling skin tissues and performing histological staining, and Mr. Masaaki Hasegawa for his support with handling pig skin tissues. We also thank Prof. Tetsuji Hirao, Dr. Toshihiko Hibino, Dr. Chika Katagiri, and Prof. Hajime Iizuka for helpful discussions.

References

- F. J. Ebling, "The normal skin," in *Textbook of Dermatology*, 3rd ed., A. Rook, D. S. Wilkinson, and F. J. G. Ebling, Eds., pp. 5–30, Wiley, John & Sons, Inc., Hoboken, New Jersey (1979).
- A. V. Rawlings, "Molecular basis for stratum corneum maturation and moisturization," *Br. J. Dermatol.* **171**(Suppl. 3), 19–28 (2014).
- A. Ishida-Yamamoto et al., "Lamellar granule secretion starts before the establishment of tight junction barrier for paracellular tracers in mammalian epidermis," *PLoS One* **7**(2), e31641 (2012).
- M. Yamamoto-Tanaka et al., "Multiple pathways are involved in DNA degradation during keratinocyte terminal differentiation," *Cell Death Dis.* **5**, e1181 (2014).
- A. Kubo et al., "External antigen uptake by Langerhans cells with reorganization of epidermal tight junction barriers," *J. Exp. Med.* **206**(13), 2937–2946 (2009).
- J. Hosoi et al., "Regulation of Langerhans cell function by nerves containing calcitonin gene-related peptide," *Nature* **363**(6425), 159–163 (1993).
- M. Tomura et al., "Tracking and quantification of dendritic cell migration and antigen trafficking between the skin and lymph nodes," *Sci. Rep.* **4**, 6030 (2014).
- M. Merad, F. Ginhoux, and M. Collin, "Origin, homeostasis and function of Langerhans cells and other langerin-expressing dendritic cells in living animals," *Nat. Rev. Immunol.* **8**(12), 935–947 (2008).
- R. E. Frugé et al., "Real-time visualization of macromolecule uptake by epidermal Langerhans cells in living animals," *J. Invest. Dermatol.* **132**, 609–614 (2012).
- G. Egawa, Y. Miyachi, and K. Kabashima, "Identification of perivascular adipose tissue in the mouse skin using two-photon microscopy," *J. Invest. Dermatol.* **70**(2), 139–140 (2013).
- K. Kabashima and G. Egawa, "Intravital multiphoton imaging of cutaneous immune responses," *J. Invest. Dermatol.* **134**, 2680–2684 (2014).
- M. Rajadhyaksha et al., "In vivo confocal scanning laser microscopy of human skin: melanin provides strong contrast," *J. Invest. Dermatol.* **104**, 946–952 (1995).
- K. Koenig and I. Riemann, "High-resolution multiphoton tomography of human skin with subcellular spatial resolution and picosecond time resolution," *J. Biomed. Opt.* **8**(3), 432–439 (2003).
- N. D. Gladkova et al., "In vivo optical coherence tomography imaging of human skin: norm and pathology," *Skin Res. Technol.* **6**(1), 6–16 (2000).
- M. D. Resch et al., "In vivo confocal microscopic imaging of the cornea after femtosecond and excimer laser-assisted penetrating keratoplasty," *J. Refractive Surg.* **31**(9), 620–626 (2015).
- P. J. Caspers et al., "In vivo confocal Raman microspectroscopy of the skin: noninvasive determination of molecular concentration profiles," *J. Invest. Dermatol.* **116**(3), 434–442 (2001).
- M. Egawa and H. Tagami, "Comparison of the depth profiles of water and water-binding substances in the stratum corneum determined *in vivo* by Raman spectroscopy between the cheek and volar forearm skin: effects of age, seasonal changes, and artificial forced hydration," *Br. J. Dermatol.* **158**(2), 251–260 (2008).
- M. Egawa et al., "In vivo characterization of the structure and components of lesional psoriatic skin from the observation with Raman spectroscopy and optical coherence tomography," *J. Dermatol. Sci.* **57**(1), 66–69 (2010).
- T. Ichimura et al., "Visualizing the appearance and disappearance of the attractor of differentiation using Raman spectral imaging," *Sci. Rep.* **5**, 11358 (2015).
- P. Piredda et al., "Subcellular Raman microspectroscopy imaging of nucleic acid and tryptophan for distinction of normal human skin cells and tumorigenic keratinocytes," *Anal. Chem.* **87**(13), 6778–6785 (2015).
- M. E. Darvin et al., "In vivo/ex vivo targeting of Langerhans cells after topical application of the immune response modifier TMX-202: confocal Raman microscopy and histology analysis," *J. Biomed. Opt.* **21**(5), 055004 (2016).
- J. X. Cheng and X. S. Xie, *Coherent Raman Scattering Microscopy*, CRC Press, Taylor & Francis Group Ltd., Oxford, United Kingdom (2012).
- C. L. Evans and X. S. Xie, "Coherent anti-stokes Raman scattering microscopy: chemical imaging for biology and medicine," *Annu. Rev. Anal. Chem.* **1**, 883–909 (2008).
- C. W. Freudiger et al., "Label-free biomedical imaging with high sensitivity by stimulated Raman scattering microscopy," *Science* **322**(5909), 1857–1861 (2008).
- P. Nandakumar, A. Kovalev, and A. Volkmer, "Vibrational imaging based on stimulated Raman scattering microscopy," *New J. Phys.* **11**, 033026 (2009).
- Y. Ozeki et al., "Analysis and experimental assessment of the sensitivity of stimulated Raman scattering microscopy," *Opt. Express* **17**(5), 3651–3658 (2009).
- M. C. Wang et al., "RNAi screening for fat regulatory genes with SRS microscopy," *Nat. Methods* **8**(2), 135–138 (2011).
- M. B. Roeffaers et al., "Label-free imaging of biomolecules in food products using stimulated Raman microscopy," *J. Biomed. Opt.* **16**(2), 021118 (2011).
- J. L. Suhalim et al., "Characterization of cholesterol crystals in atherosclerotic plaques using stimulated Raman scattering and second-harmonic generation microscopy," *Biophys. J.* **102**, 1988–1995 (2012).
- Y. Ozeki et al., "High-speed molecular spectral imaging of tissue with stimulated Raman scattering," *Nat. Photonics* **6**, 845–851 (2012).
- D. Zhang et al., "Quantitative vibrational imaging by hyperspectral stimulated Raman scattering microscopy and multivariate curve resolution analysis," *Anal. Chem.* **85**(1), 98–106 (2013).
- L. Wei et al., "Vibrational imaging of newly synthesized proteins in live cells by stimulated Raman scattering microscopy," *Proc. Natl. Acad. Sci.* **110**(28), 11226–11231 (2013).

33. L. Wei et al., "Live-cell imaging of alkyne-tagged small biomolecules by stimulated Raman scattering," *Nat. Methods* **11**(4), 410–412 (2014).
34. D. Fu et al., "In vivo metabolic fingerprinting of neutral lipids with hyperspectral stimulated Raman scattering microscopy," *J. Am. Chem. Soc.* **136**(24), 8820–8828 (2014).
35. D. Fu et al., "Imaging the intracellular distribution of tyrosine kinase inhibitors in living cells with quantitative hyperspectral stimulated Raman scattering," *Nat. Chem.* **6**(7), 614–622 (2014).
36. S. Satoh et al., "Label-free visualization of acetaminophen-induced liver injury by high-multivariate image analysis," *Pathol. Int.* **64**(10), 518–526 (2014).
37. J. X. Cheng and X. S. Xie, "Vibrational spectroscopic imaging of living systems: an emerging platform for biology and medicine," *Science* **350**(6264), aaa870 (2015).
38. W. S. Chur et al., "Molecular diffusion in the human nail measured by stimulated Raman scattering microscopy," *Proc. Natl. Acad. Sci. U. S. A.* **112**(25), 7725–7730 (2015).
39. Y. Otsuka et al., "On-line visualization of multicolor chemical images with stimulated Raman scattering spectral microscopy," *Analyst* **140**(9), 2984–2987 (2015).
40. S. Yue and J. X. Cheng, "Deciphering single cell metabolism by coherent Raman scattering microscopy," *Curr. Opin. Chem. Biol.* **33**, 46–57 (2016).
41. B. G. Saar et al., "Video-rate molecular imaging *in vivo* with stimulated Raman scattering," *Science* **330**(6009), 1368–1370 (2010).
42. B. G. Saar et al., "Imaging drug delivery to skin with stimulated Raman scattering microscopy," *Mol. Pharmaceutics* **8**(3), 969–975 (2011).
43. D. M. Drutis et al., "Three-dimensional chemical imaging of skin using stimulated Raman scattering microscopy," *J. Biomed. Opt.* **19**(11), 111604 (2014).
44. F. K. Lu et al., "Label-free DNA imaging *in vivo* with stimulated Raman scattering microscopy," *Proc. Natl. Acad. Sci. U. S. A.* **112**(37), 11624–11629 (2015).
45. I. Boudry et al., "Percutaneous penetration and absorption of parathion using human and pig skin models *in vitro* and human skin grafted onto nude mouse skin model *in vivo*," *J. Appl. Toxicol.* **28**(5), 645–657 (2008).
46. K. Kawabata et al., "The presence of N(ϵ)-(carboxymethyl) lysine in the human epidermis," *Biochim. Biophys. Acta (BBA)—Proteins Proteomics* **1814**(10), 1246–1252 (2011).
47. S. W. Thompson, *Selected Histochemical and Histopathological Methods*, p. 1639, Charles C Thomas Publisher Ltd., Springfield, Illinois (1966).
48. N. Yasmin et al., "Identification of bone morphogenetic protein 7 (BMP7) as an instructive factor for human epidermal Langerhans cell differentiation," *J. Exp. Med.* **210**(12), 2597–2610 (2013).

Mariko Egawa is a research scientist in Life Science Research Center at Shiseido Co., Ltd. Japan. She has focused her research on the application of spectroscopy techniques, including near-infrared spectroscopy, spontaneous Raman scattering microscopy, and coherent Raman scattering microscopy, for evaluation of skin functions and conditions. She has published more than 25 peer-reviewed papers in international journals on topics such as noninvasive optical skin analysis.

Yasuyuki Ozeki is an associate professor of Electronic Engineering and Information Systems at University of Tokyo, Japan. He has been working on photonic techniques for generation, control, and measuring optical pulses and on nonlinear-optical microscopy techniques including stimulated Raman scattering microscopy. He is the authors of more than 50 scientific publications on international peer-reviewed journals.

Biographies for the other authors are not available.